Comprehensive study of initial diameter effects and other observations on convection-free droplet combustion in the standard atmosphere for *n*-heptane, *n*-octane, and *n*-decane☆

Yu Cheng Liu [a,1], Yuhao Xu [b], Michael C. Hicks [c], C. Thomas Avedisian [b,*]

[a] Department of Computer Science, Engineering and Physics University of Michigan-Flint, MI 48502, USA
[b] Sibley School of Mechanical and Aerospace Engineering Cornell University, Ithaca, NY 14853, USA
[c] NASA-Glenn Research Center, Combustion and Reacting Systems Branch, Cleveland, OH, 44135, USA

ARTICLE INFO

ABSTRACT

This paper reports the results of a comprehensive experimental study on the effect of initial droplet diameter (D_o) over a very wide range ($0.5\,\text{mm} < D_o < 5\,\text{mm}$) on the spherically symmetric droplet burning characteristics in the standard atmosphere of three alkanes – *n*-heptane, *n*-octane and *n*-decane – that are representative of components found in petroleum-based transportation fuels and their surrogates. Spherical symmetry in the burning process was promoted by carrying out the experiments in a reduced convection (stagnant ambience) and buoyancy (low gravity) environment using the facilities of a ground-based drop tower for $D_o < 0.8\,\text{mm}$ and a spaced-based platform (the International Space Station) for $D_o > 1.0\,\text{mm}$.

The results show that for D_o greater than about 2 mm, K decreases with increasing D_o in an early period of burning and with the data being correlated in the form $K \sim D_o^{-n}$ based on a scale analysis of an energy balance on the flame. For D_o larger than approximately 2 mm the droplet flames often disappeared indicating an extinction mechanism that was speculated to be due to radiative losses from the flame. Concurrently, measurements of wideband radiation dropped significantly and the burning rate gradually approached pure evaporation.

In some instances for *n*-heptane and *n*-octane radiative extinction was accompanied by droplet evaporation rates that were significantly higher than evaporation in a hot ambience which persisted for a significant fraction of the burning history before decreasing to evaporation in a cold ambience. An energy balance on the drop related the flame temperature to droplet diameter from which it was predicted that flame temperatures after ignition were greater than 1200 K before dropping to under approximately 800 K and remaining constant thereafter until eventually reaching near ambient conditions. This intermediate regime of burning was conjectured to be associated with a low temperature combustion process. The transition to this intermediate regime upon radiative extinction was occasionally accompanied by flame oscillations, the origin of which was uncertain but could have been initiated by motion of the droplet owing to the deployment process.

© 2016 The Combustion Institute. Published by Elsevier Inc. All rights reserved.

1. Introduction

Droplet combustion is an important scientific problem as it relates to the earliest theoretical treatments of liquid combustion which assumed spherical symmetry [1,2]. For this configuration,

the droplet and flame are concentric and the gas flow is due entirely to evaporation. Figure 1a is a schematic of the combustion symmetry that results. If soot is produced during the burning process the aggregates will be trapped between the droplet and flame by a balance of the inwardly directed thermophoretic force and outwardly directed drag force due to evaporation of the fuel [3,4]. The soot shell that results is porous spherical shell-like structure. An illustrative example of this for *n*-decane is shown in the photograph of Fig. 1b at one instant of its burning history.

The classical theory of droplet combustion leads to a scaling for the droplet diameter and time in the form
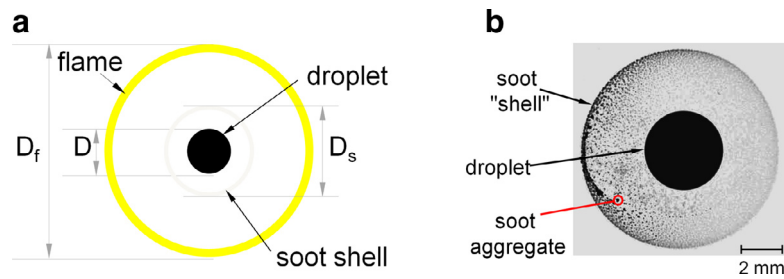
Fig. 1. (a) Schematic (not to scale) of a spherically symmetric droplet flame with the flame, soot shell, and droplet concentric to each other, which is the canonical configuration for droplet combustion. (b) Zoomed-in photograph of a free-floating and stationary *n*-decane droplet burning in the standard atmosphere showing the combustion symmetry that results when external convective influences are minimal. The soot shell is a porous entity. Soot aggregates are trapped to form the shell by the forces acting on the aggregates (the flame for (b), not visible, is about ten times the droplet diameter).

Nomenclature

C_D	parameter related to collision integral, characteristic molecular length, and universal gas constant ($kg^{1/2}$ $mol^{1/2}/(s\ m\ K^{1/2})$)
C_F	conversion factor for length, $= D_f/D$ (–)
D	droplet diameter (mm)
$\wp$	diffusion coefficient (m^2/s)
g	gravity (m/s^2)
h_{fg}	heat of evaporation (J/kg)
K	droplet burning or evaporation rate (mm^2/s, or m^2/s)
k	thermal conductivity (W/(m K))
M_W	molecular weight (g/mol)
$\dot{m}_F$	mass transfer rate of fuel (kg/s)
P	pressure (Pa)
$\dot{Q}$	heat transfer rate (J/s)
Ra	Rayleigh number
Re	Reynolds number
T	temperature (K)
t	time (s)
U	velocity (m/s)

Greek letters

α	thermal diffusivity (m^2/s)
β	thermal expansion coefficient (1/K)
ΔH_c	heat of combustion (J/kg)
ε	emissivity (–)
κ	absorption coefficient (1/m)
ν	kinematic viscosity (m^2/s)
ρ	density (kg/m^3)
σ	Stefan-Boltzmann constant (W/($m^2\ K^4$))
ξ	ratio of time scales (–)

Subscripts

b	burning
boil	boiling
c	critical condition
comb	combustion
cond	conduction
d	droplet
ext	extinction
f	flame
g	gas phase
h	thermal
in	inward direction
L	liquid phase
melt	melting
o	initial value
out	outward direction

r	relative
rad	radiation
res	residence
rxt	radiative extinction threshold
s	soot

$$\left(\frac{D}{D_o}\right)^2 = 1 - K\left(\frac{t}{D_o^2}\right) \tag{1}$$

where K is the "burning rate",

$$K \equiv \left|\frac{d(D/D_o)^2}{d\left(t/D_o^2\right)}\right|. \tag{2}$$

Furthermore, the relative position of the droplet surface to the flame, or the flame "standoff" ratio (D_f/D) is predicted to be a constant. These outcomes are not consistent with the reported measurements. Regarding soot, the theory assumes a single step reaction and, thus, has no capacity to predict formation of soot precursors or a soot shell, though it will be expected that soot forms on the fuel-rich side of the flame and that the relative position of the soot shell diameter to the droplet surface, or the soot standoff ratio (D_s/D), will track with the flame position.

Extensions to the spherically symmetric theory have incorporated a wide range of processes to explain some of the effects neglected by the classical theory, such as transient droplet heating, variable properties, non-luminous radiation, and detailed combustion chemistry [5–11]. The inclusion of detailed combustion chemistry is particularly significant because it provides the capability to address soot formation through prediction of its precursors (e.g., acetylene, polycyclic aromatic hydrocarbons, etc.) [3,12–15]. The results of these detailed numerical treatments show that the droplet burning process is inherently unsteady, with the burning rate exhibiting a time dependence that originates in liquid phase unsteadiness persisting throughout burning[2] or flame extinction mechanisms that force the burning rate to decrease near the end of burning, with the flame standoff ratio continually increasing with time. Experimental observations confirm predictions of these effects from detailed numerical modeling [8–11].

Though the burning rate is predicted to be constant and independent of time and droplet size, experiments show that the burning rate decreases as the initial droplet diameter increases and that it depends on time [3,13,14,16–31]. This trend has not been fully

---

[2] Transient droplet heating may be explained by comparing the characteristic time for thermal diffusion, $t_h \sim D_o^2/\alpha_L$, to the droplet burning time, t_b: $\xi_h = \frac{t_h}{t_b} \sim \frac{K}{\alpha_L}$. Using properties representative of hydrocarbon fuels, (e.g., $\alpha_L \sim 10^{-8}\ m^2/s$, $K \sim 10^{-6}\ m^2/s$) shows that $\xi_h >> 1$ which suggests that transient heating effects can persist throughout the droplet lifetime regardless of the droplet size.
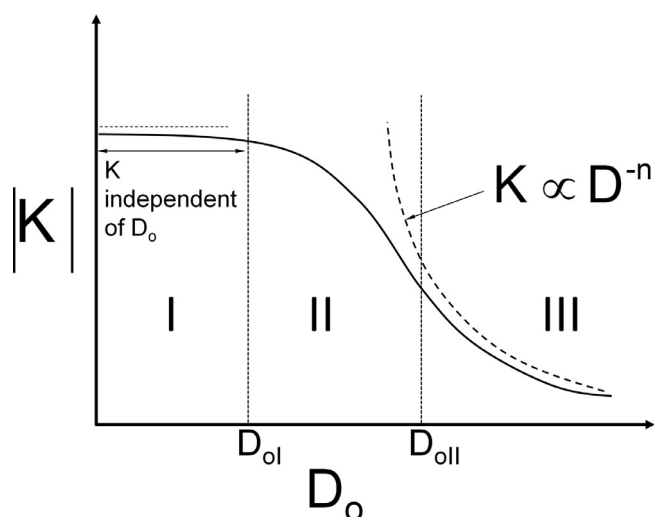
Fig. 2. Schematic of dependence of burning rate on D_o for a droplet burning in a cold ambience (see Appendix A). When radiation is neglected (region I) the burning rate is indicated as being independent of D_o; when radiative losses are important K decreases with D_o (region II and III).

Fig. 3. Schematic of postulated influences of an initial diameter (D_o) on burning rate (K).

Table 1
Selected properties for *n*-heptane, *n*-octane, and *n*-decane.

	n-Heptane	*n*-Octane	*n*-Decane
Chemical formula [a]	C_7H_{16}	C_8H_{18}	$C_{10}H_{22}$
M_W (g/mol) [a]	100.21	114.23	142.29
T_{boil} (K) [a]	371.6	398.8	447.3
T_{melt} (K) [a]	182.6	216.4	243.5
ρ_L @ 293 K (kg/m^3) [b]	684	703	730
ρ_L @ T_{boil} (kg/m^3) [b]	608	605	609
T_c (K) [a]	540.2	568.8	617.6
P_c (atm) [a]	27	24.5	20.8
h_{fg} (kJ/kg) [c]	316	300	277
HHV (kJ/kg) [c]	48,456	48,275	48,020
LHV (kJ/kg) [c]	44,926	44,791	44,602
$T_{f,ad}$ (K) [c]	2273	2275	2277

[a] Ref. [44].
[b] From Tyn/Calus method in Ref. [44].
[c] Ref. [2]; HHV = higher heating value, LHV = lower heating value.

explained, owing in part to the inability to model all of the important processes in droplet burning (i.e., unsteady transport, variable properties, soot formation, radiation, complex combustion chemistry). Scale analysis [32,33] as applied to droplet burning offers capabilities to develop an understanding of the important variables involved. Appendix A discusses this approach. Three regimes of burning based on D_o are identified as depicted in a schematic form in Fig. 2, based on heat transfer from the flame to the droplet and ambience in terms of radiation and conduction transport. A single burning rate for a given droplet history is an outcome of the theory, though in fact K is often time dependent owing to unsteady heating and various extinction mechanisms (e.g., diffusive and radiative mechanisms, and transitions to low temperature combustion (LTC) or "cool flame" regimes of burning) that may arise during the burning process.

Neglecting radiation (regime I in Fig. 2), the scale analysis presented in Appendix A leads to the burning rate being independent of D_o. This trend is consistent with detailed numerical modeling that also predicts K to be independent of D_o [8,13]. This approximation would remain in effect for droplet sizes down to those found in sprays [33–36]. The upper bound of droplet diameter for radiation to be unimportant is indicated as D_{oI} in Fig. 2 where the soot shell will not form due to small residence times [3]. For large D_o where radiative losses from the flame to the ambience are more important than diffusive transport (regime III) an energy balance (discussed in Appendix A) on the flame leads to an inverse power relationship, $K \propto D_o^{-n}$ ($n = 2/7$ from the scaling analysis). Effects such as radiative extinction [9,25,36] and LTC phenomena as first postulated by Nayagam et al. in 2015 [37] and subsequently analyzed with detailed numerical modeling [38–41] may also be important in this regime. An intermediate regime where both radiation and diffusive transport are important would bridge regimes I and III. Figure 3 summarizes the postulated influences of D_o on K through various convoluted phenomena that may occur during a dynamic droplet burning process.

Scale analysis does not provide quantitative information about the boundaries for the various regimes in Fig. 2. Such information will come mainly from experiment and detailed numerical modeling. The limited data suggest that $D_{oI} \sim 1$ mm. The upper range (D_{oII}) is unknown though probably in the range of 2 mm [33]. One of the purposes of the present investigation is to examine the droplet burning process over the widest range
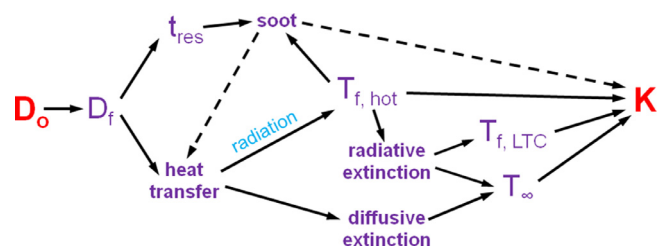
0.5 mm $< D_o <$ 5 mm to elucidate various regimes of burning. Measurements made across such a large range of D_o as reported in this study will also be valuable to test the ability of detailed *ab initio* numerical models of liquid fuel combustion that assume the base case of Fig. 1 [8–12,15,41,42]. It is important to note that the motivation for studying the burning process of the large droplets at the upper end of this range in no way is meant to suggest the relevance of droplets for $D_o \sim 5$ mm to practical spray systems. To the contrary, typical D_o values in spray flames are on the order of 100 μm or less, which would be most relevant to regime I in Fig. 2 which extends to about $D_o \sim 1$ mm. On the other hand, the physical processes that emerge to control burning as D_o increases are very much relevant to combustion of spray systems even if the actual droplet diameters are not.

The virtue of examining the droplet burning process in the context of Fig. 1 is, therefore, to provide quantitative measurements over the widest possible range of D_o with the available consistent experimental facilities. The understanding of processes known to exist in large (e.g., spray) systems can still be derived from observations on the scale of individual isolated droplets, where it is recognized that moving boundary, radiative and unsteady transport dynamics remain as the length scale of a spray is reduced to the base case of spherical symmetry [7].

The fuels employed in the present study are *n*-heptane, *n*-octane, and *n*-decane. A selected set of properties is given in Table 1. Their detailed combustion chemistry is relatively well-developed and they are representative of a chemical class that is prominent in real transportation fuels [43]. Being also in a series of straight chain hydrocarbons the results will facilitate an understanding of how hydrocarbons in such a series burn and respond to changes across the wide range D_o investigated.

2. Promoting spherical symmetry for droplet burning

The droplet burning configuration of interest here is depicted in Fig. 1. Its development relies on reducing the relative velocity between the droplet and ambience, whether by forced convective or

buoyancy flows. The relevant dynamic parameters are the Reynolds number, $Re = \frac{U_r D_o}{\nu}$, and the Rayleigh number, $Ra = \frac{g\beta(T_f - T_d)D_o^3}{\alpha\nu}$. Both should be "small". A small velocity U_r is achieved by ensuring that the test droplet experiences minimal drift during the combustion process. Two experimental designs that accomplish this are presented in Section 3. In one, the test droplets are physically anchored to very small support fibers, and in the other a delicate deployment design creates free-floating and near stationary droplets. To reduce the influence of buoyancy, the experiments are performed in a low gravity environment. The alternative of doing experiments in a low pressure ambience was not considered because it would also reduce the sooting propensity that is an important element of the present study.

A low gravity environment is achieved by carrying out the experiments under free-fall conditions in a gravitational field. The test droplet is deployed in a sealed chamber containing the desired combustion gases (room temperature air in the present study) and the associated instrumentation is then literally placed into free-fall while test droplets are burned. This state of free fall is realized in facilities on the ground ("ground-based" (GB)) and within the environment of the International Space Station (ISS).

The need for GB and ISS facilities is motivated by the range of droplet sizes of interest and their corresponding burning times, and hardware capabilities. For $0.5\,\text{mm} < D_o < 5\,\text{mm}$ the required burning times would ostensibly range from approximately 0.3 to 50 s (i.e., $t_b \sim D_o^2/K$ for burning rates between $0.5\,\text{mm}^2/\text{s}$ to $0.7\,\text{mm}^2/\text{s}$ which is typical of hydrocarbons burning in the standard atmosphere). For the ISS the experimental time is unlimited and virtually any size droplet can be examined, though the droplet deployment hardware is not optimized for $D_o \sim 1\,\text{mm}$ owing to the challenge of deploying droplets with minimum drift with the current experimental design (Section 3.1). For $D_o < 1\,\text{mm}$, a GB drop tower is employed that provides 1.2 s of free fall which is suitable for observing the complete burning history of droplets up to about 0.8 mm.

The gravity level in the moving frame of reference is commensurate with the air drag around the instrumentation package within which the experiments are carried out. For the GB configuration the effects of air drag are minimized by placing the inner package containing the hardware within a larger outer box (a so-called "drag shield") that falls independently of the inner package. In the ISS, the orbital trajectory (at about 205 miles) is of such an elevation that the low pressure gases surrounding the ISS platform do not exert any significant air drag on the ISS. For the GB and ISS environments, the gravitational field – $g/g_o < \sim 10^{-4}$ – is sufficient [3,17,26,45] to promote a near one-dimensional transport dynamic. The soot shell formed in such a gravitational condition is clearly visible (cf. Fig. 1b) and soot aggregates trapped between the droplet and flame exhibit spherical symmetry under ideal conditions. Deviations from this state of combustion symmetry would be due to extraneous effects associated with ignition disturbances, drift of the droplets (for the free-floating drops of the ISS), and fiber influences (for the GB studies).

In the present study, the burning dynamics of a wide range of initial droplet diameters are investigated: $0.5\,\text{mm} < D_o < 0.8\,\text{mm}$ in a GB drop tower; and $1.2\,\text{mm} < D_o < 5\,\text{mm}$ in the ISS. This range would constitute the largest thus far reported in a single study.

3. Experimental methods

3.1. International space station

An experimental design was developed to form, deploy and ignite free-floating droplets in the low gravity environment of the ISS. The droplet combustion hardware (i.e., the Multi-user Droplet
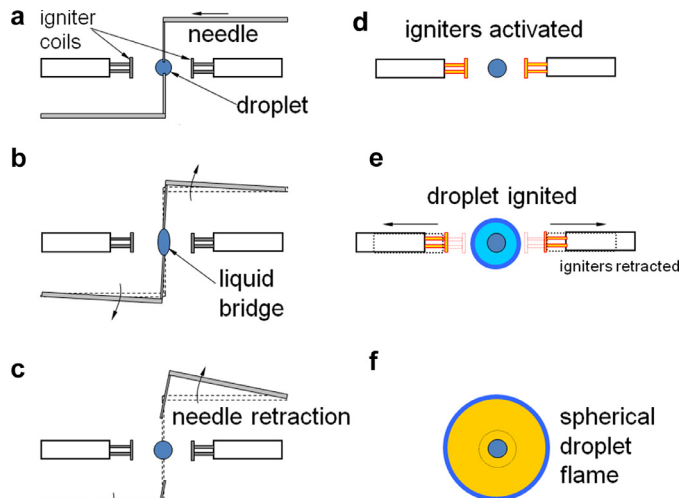

Fig. 4. Steps to form, deploy and ignite an unsupported droplet in the Multi-user Droplet Combustion Apparatus (MDCA) within the ISS: (a) fuel deployment; (b) formation of liquid bridge by increasing the distance between the two needle tips; (c) needle retraction to leave behind a droplet; (d) igniter coils activated; (e) droplet ignition, igniters retracted; (f) droplet burning.

Combustion Apparatus (MDCA)) is housed within the "Combustion Integrated Rack" (CIR) of the ISS. An outline of the hardware and procedures are presented here. More details of the hardware design have been provided elsewhere [46–48].

The ISS instrumentation package includes video cameras to record the droplet deployment, ignition, and droplet burning process. The main diagnostic of the experiments is digital video imaging. Three digital video cameras were used with all operating at 30 fps. A high bit depth/multispectral (HiBMs) camera records black and white silhouette images of the droplet and soot shell; a color camera records flame-illuminated images that illustrate the boundary of the outer luminous zone of the flame from which the "flame" diameter is obtained; and a low-light-level ultraviolet (LL-LUV) camera captures the 310 nm OH emission spectra as an alternative marker of the flame position. A wideband and a narrowband radiometer (recorded at 100 Hz) were also used to signify emission of visible and invisible flames. For all experiments, images from each of these cameras are analyzed for each experimental run.

The experiments are carried out in a sealed combustion chamber that is charged with the standard atmosphere (other inerts besides nitrogen can be accommodated as well). The MDCA was designed to provide unsupported or free-floating droplets with minimal drift to promote combustion symmetry. Once ignited the droplet burning process is recorded by the video cameras, and the results are temporarily stored in the data storage units on the ISS until scheduled downlink events.

A number of designs have been developed for forming and deploying free-floating droplets for combustion experiments [49]. The one in the MDCA is schematically illustrated in Fig. 4a–f and described in [48]. Briefly, test droplets are formed by first dispensing fuel through two opposed (250 μm diameter) needles with polished and fluted ends, and separated by a small distance to create a liquid bridge (Fig. 4b). The liquid bridge is stretched slightly and the needles are then rapidly retracted (Fig. 4c) at the same speed. The liquid bridge left behind quickly collapses into a spherical droplet (Fig. 4c) after a small period of oscillation at which point the now free-floating (and nearly stationary) droplet is ready to be ignited (Fig. 4d). The ignition process is accomplished by rapid heating of the gases near to the droplet by hot wires that are energized shortly after the needles are retracted (Fig. 4e). There-
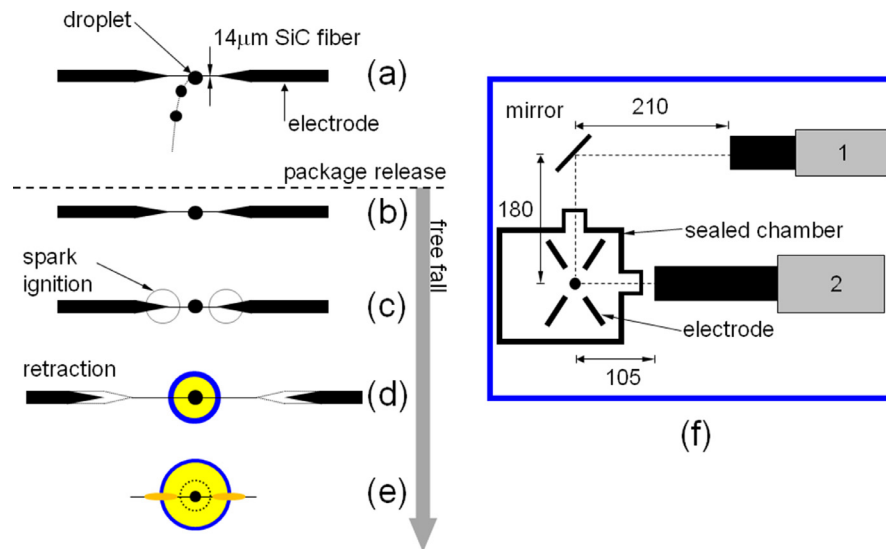
Fig. 5. Illustration of design for forming, deploying and spark-igniting droplets in the ground-based facility where low gravity is achieved over a 7.6 m free-fall. (a) droplet deployment by a piezoelectric generator at the intersection of two crossed SiC fibers (view is on-plane) followed by package release (b), spark activation (c), electrode retraction (d), and burning (e). Component layout of instrumentation package (f), which is in free-fall. Numbers are in mm. Hardware to accomplish a–e is mounted in sealed chamber. Camera '1' is a Hitachi HV-C20 color camera (0.3 MP/frame, 30 fps); camera '2' is a Canadian Photonics Laboratory MS-80 K black and white camera (3.9 MP/frame, 200 fps).

after, the droplet burns in an unobstructed ambience (Fig. 4f) to produce the sort of combustion symmetry shown in Fig. 1a.

Several adjustments are often found necessary in order to minimize drift of the droplet during deployment. For instance, the distance between the needle tips prior to droplet deployment and the duration over which the hot wires are energized influence the droplet trajectory. In general, igniters are positioned more distantly to accommodate larger droplets. Ignition for fuels with a higher boiling point (e.g. *n*-decane) requires higher power or longer igniter charging.

The experiment was controlled remotely by a team at the NASA-Glenn Research Center (Cleveland, Ohio) through transmissions that passed through the NASA Space Flight Center (Huntsville, Al), the NASA Johnson Space Flight Center (Houston, TX), the White Sands Test Facility (Las Cruces, NM), the in-orbit Tracking and Data Relay Satellite System and finally to the ISS. Concurrently, a video feed that showed the MDCA on the ISS in real time was transmitted to both NASA-Glenn and Cornell University (in Ithaca, N.Y.). The Cornell investigators provided real-time input via a phone link between Cornell and NASA-Glenn as related hardware settings of the experiment (e.g., droplet size conditions power to the igniters, spacing between the deployment needles, positioning of the ignition coils, etc.).

3.2. Ground-based experimental design

A small-scale 1.2 s (7.6 m) drop tower [50] was used to study the droplet burning history for $D_o < 0.8$ mm. Details of the droplet deployment and ignition arrangement are described in Ref. [27]. The experimental design employs a small diameter (14 μm) SiC fiber on which test droplets are placed to restrict their motion; alternatively, the fibers can be removed to develop free-floating droplets [17,50–52].

The facility consists of an instrumentation package which contains the droplet deployment arrangement and cameras are enclosed by a drag shield that minimized the effects of air drag during free fall for the inner instrumentation package. The instrumentation package is placed in free-fall to achieve low gravity in the moving frame of reference during which the experiments are carried out. Gravity levels in the moving frame of reference were about 10^{-4} of earth's gravity. Signals and commands are transmit-

ted from the equipment on the PC table through a multi-wire cable into the instrumentation package. The cable hangs from the bottom of the package while the instrumentation package falls over the 7.6 m distance to give an experimental time of about 1.2 s.

Figure 5f shows the positions of the imaging cameras used to record the droplet burning process. A black and white (BW) camera (Canadian Photonic Labs, MS-80K) records the backlit droplet and soot shell at 200 fps with an image quality of 3.9 MP/frame. A color camera (Hitachi HV-C20) records self-illuminated images of the droplet flames at 30 fps with a quality of 0.3 MP/frame. The following lenses are fitted on a C-mount adapter installed on the BW camera: an Olympus Zuiko 90 mm f/2.0 lens, an Olympus OM Telescopic Extension Tube 65–116 mm (fixed at 100 mm), and a Vivitar MC 2X teleconverter. For the color camera, a Nikkor 135 mm f/2.0 lens and two Kenko 36 mm extension tubes were used.

To deploy a droplet onto the support fibers, a droplet generator propels one or more droplets from the nozzle onto two 14 μm SiC fiber filaments (Fig. 5a) that are crossed at 60° until the droplet reaches the desired size. With the test droplet positioned at the intersection of the two fibers, the entire package is released into free-fall by deactivating an electro-magnet that initially held the package to initiate a low gravity experiment (Fig. 5b). During the fall, the droplet is ignited by two parallel sparks across two pairs of electrodes (Fig. 5c) that retract immediately after ignition (Fig. 5d) leaving an isolated droplet flame ready for imaging (Fig. 5e). The test droplets were ignited 300 ms after the period of free-fall began to eliminate a shaking affect that was observed upon separation of the instrumentation package from the electromagnet.

To ensure that the fiber-mounted droplets produced results that were not substantially influenced by the support fiber (e.g., fiber-induced motion in the gas that could influence the burning rate), some limited experiments using the procedures for developing unsupported droplets in the GB facility were reported [52] for *n*-decane and compared with the fiber-mounted droplets. The results confirm earlier conclusions [17,29] that the burning rates of the freely floating and fiber mounted droplets were close to each other. On the other hand, the fiber support perturbed the soot structure and promoted aggregates to stick to the fiber during the burning process [49].
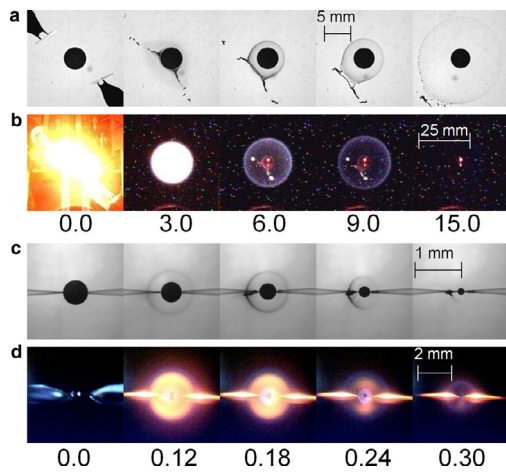
Fig. 6. Photographs showing typical burning configurations for the space-based (a, b) and ground based (c, d) experiments for an n-heptane droplet (a, b, $D_o = 4.79$ mm) and an n-decane droplet (c, d $D_o = 0.55$ mm); length scales (different for each row) are embedded. The time (s) from ignition is indicated beneath each pair of rows. Upper rows in each sequence (a, c) are backlit photographs showing development of the soot shell. Lower rows (b, d) are self-illuminated color images showing development of the flame. The rapid expansion of the soot cloud from (a: 9.0) to (a: 15.0) is caused by flame extinction (b: 15.0). Speckles in (b) are an artifact created by the image sensor. (For interpretation of the references to colour in this figure legend, the reader is referred to the web version of this article).

Figure 6a and b shows selected images of a burning n-decane droplet ($D_O = 4.79$ mm) that illustrate the visualizations obtained from the cameras employed in the experiments from the ISS facilities. The droplet in ISS experimental run is free-floating and remains relatively stationary. The first row (Figure 6a) of images shows a series of backlit photographs from the HiBMs camera. The second row (Figure 6b) is a set of flame-illuminated images which illustrate the evolution of the flame structure. The soot and flame asymmetries in Fig. 6 are the result of the aforementioned droplet motions. The clarity of the images reveals the evolution of the soot tail as burning progresses. Eventually (last image in Fig. 6a), the shell attains a nearly spherical configuration as disturbances associated with the initial events of deployment and ignition dissipate.

Figure 6c and d shows representative images of a burning n-decane droplet with $D_O = 0.55$ mm from a GB experiment. Figure 6c is a series of backlit images showing the droplet, soot shell and fiber support. The pictures in the last row (6d) are flame-illuminated images. The bright glows on either side of the droplet are due to the hot flame intersecting with the fiber.

Though the ISS design employs hot wire ignition and the drop tower experiments used ignition by spark discharge, it was previously shown [30] that the spark and hot wire ignition approaches gave very similar results. The minimum amount of energy to just ignite test droplets was employed. Similarly, for the large droplet data reported here an attempt was made to keep the ignition coil energy to a minimum needed to ignite droplets.

3.3. Image analyses and data reduction

Critical to acquiring quantitative measurements is the ability extract the droplet (D), soot shell (D_s) and flame (D_f) from the individual digital video images. The process is laborious. It combines approaches that employ computer algorithms and manual operations. The data extraction processes are discussed in detail elsewhere [27,43,53]. For the experiments carried out for this paper, over 8000 raw images were analyzed. A subset of these images was used to construct the evolutions of D, D_f and D_s presented in Section 4.

Figure 7a shows an image that illustrate the droplet boundary identified by the image analysis software (outlined by red dashed line around the droplet boundary) by the automated process described in Ref. [53]. From the same BW images, soot shell diameters are measured in a manual process using a commercial software package (Image-Pro Plus v6.3) that is used to place a circle around the droplet or soot shell. Figure 7a also illustrates the technique to identify the soot "circle" or "ellipse" (in a 2D image) as outlined by blue dashed line. The droplet and soot shell diameters are then extracted from the identified geometry (a circle or an ellipse). There may exist some asymmetric part of the soot shell (e.g., Fig. 6a). This asymmetry comes from either early soot shell distortion (due to ISS igniters retraction) or incident soot aggregation at one angle such that it has less physical meaning regarding the position where the soot particles are situated as a result of the "force balance" between Stefan drag, diffusio-phoresis and thermophoresis [12,54,55]. The non-spherical part of soot shell is therefore excluded and the circle extended around the circumference. It is important to note that the hydrocarbons investigated in this study produce soot almost everywhere within the flame area. The soot shell diameter only indicates where very small soot particles (instead of more massive soot aggregates) are positioned inside the spherically symmetric flame.

Typical flame-illuminated images (for a sooting and non-sooting flame, respectively) are shown in Figure 7b and c. These images were obtained from the color camera without any back illumination. Measurements of D_f were extracted from such images by manually positioning a virtual ellipse (dashed circle) around the outer blue zone of the bright central core (originating from incandescence of soot aggregates) with the aid of the Image-Pro software. Figure 7d shows an LLLUV image (again, without any backside illumination) that reveals the boundary of OH emissions (dashed circle) at the same instant as in Fig. 7c (the scale for Fig. 7c is the same as d). The flame diameters obtained from the LLLUV images were always consistently larger compared to D_f values obtained from color images. In the present study, the D_f data presented are obtained only from the color images (i.e., Fig. 7b and c).

For ISS apparatus and commensurate with the camera used in the MDCA, the uncertainty of the droplet boundary was assessed at ±5 pixels (or ±0.15 mm; counting the boundary thickness on both ends of a diameter). For $D \sim 5$ mm (156 pixels), the measured droplet size would then have an uncertainty of ±3.2%. The smallest droplet size reported here for ISS experiment is around 0.35 mm (12 pixels). The corresponding uncertainty for such a small droplet is rather large at ±41.6%, though comparatively few data extractions were performed for such small droplets in ISS video images. When droplet diameters are larger than 1 mm the uncertainty is less than 10%.

The flame diameter has an uncertainty of ±6 pixels (or ±0.87 mm). For the range of reported flame sizes (Figs. 21–23), the smallest diameter (usually at ignition) is about 8.7 mm (60 pixels) with an uncertainty of ± 10%, and the largest (usually during burning) flame diameter is about 32 mm (220 pixels) with an uncertainty of ±2.7%. The soot shell diameters measured from ISS experiments ranged from about 2.0 mm (70 pixels) to 6.2 mm (210 pixels) with an uncertainty of the thickness of the soot shell of ±3 pixels, leading to an uncertainty of D_s of between 1.4% and 4.3%.

For GB experiments with $D_o \sim 0.5$ mm, estimates of measurement uncertainty reported previously [43] range from ±2% to ±12.5% (250 to 40 pixels with an uncertainty of ±5 pixels). Soot shell diameters range from 750 to 300 pixels, and for an uncertainty of 20 pixels measurements of D_s could vary between ±3% and ±7%. The flame boundary is approximately 8 pixels thick resulting in a range of uncertainties between ±4.2% and ±8%.
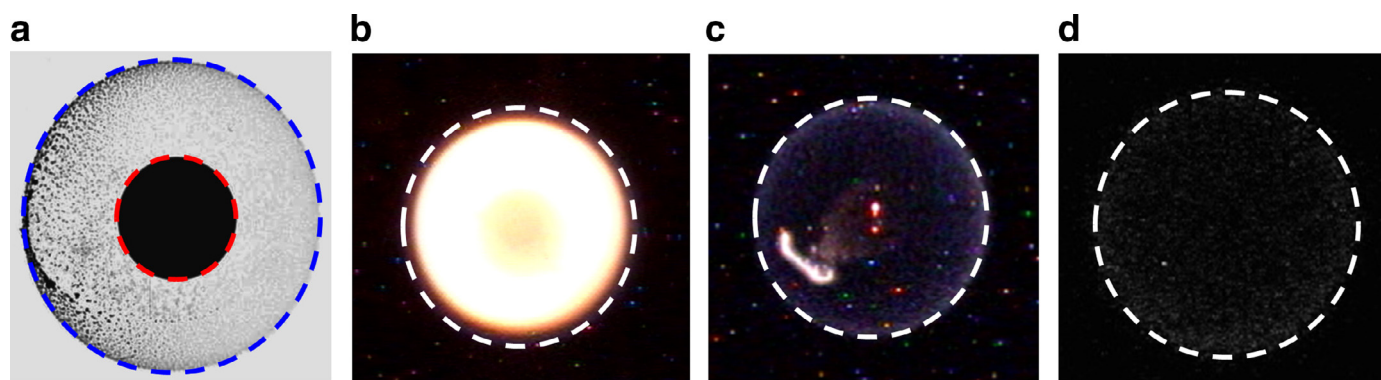
Fig. 7. Droplet and flame images illustrating placement of virtual ellipses for droplet (red), soot (blue) and flame (white) boundaries. (a) Droplet (performed by an automated program [53]) and soot shell boundary; (b) flame boundary for a bright yellow flame with the ellipse placed just outside the luminous zone; (c) flame boundary for a blue flame; (d) flame boundary for an LLLUV image showing OH emission boundaries. The images in (c) and (d) have identical length scales which show that the OH emission boundary is slightly larger than the blue flame boundary which was found for all burning conditions. The 'Supplementary materials' section includes all data extracted from these operations. (For interpretation of the references to colour in this figure legend, the reader is referred to the web version of this article).
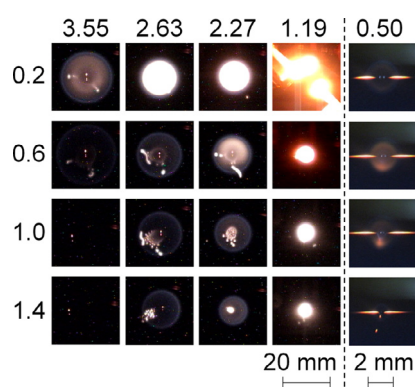
Fig. 8. Representative flame-illuminated images of burning *n*-heptane droplets. Numbers across the top are D_o (mm); numbers in column are t/D_o^2 (s/mm²). Images to the right of the dotted line are from a ground-based experiment (the droplets are supported) while images to the left are from space-based experiments (the droplets are free-floating). Note that the images from the space-based and ground-based experiments are scaled differently. (For interpretation of the references to colour in this figure legend, the reader is referred to the web version of this article).

Additional data related to radiative emissions was obtained from the voltage output of radiometers mounted inside the combustion chamber of the ISS facility. The voltage signals were converted to flame radiance (W) using a calibration developed from the power output of the hotwire igniters within a pre-defined ambient composition, pressure and temperature. Radiometer data are presented and discussed in Section 4 for selected experiments that suggest the realization of radiative extinction and LTC regimes.

4. Results and discussions

Figures 8–10 show a selected set of images of the burning histories of *n*-heptane, *n*-octane and *n*-decane, respectively. The D_o values are indicated at the top of the figures. The vertical dotted line in Figs. 8–10 separates the GB experiments ($D_o < 1$ mm) from the ISS experiments ($D_o > 1$ mm). The scale factors are indicated at the bottom of the figures. The images along any column show the burning history of droplets for the indicated D_o. The time stamps (on the left) correspond to the normalized time (t/D_o^2 (s/mm²)) of the image in the burning history. The two needle-like glows on opposite sides of the GB images are the result of the fiber passing through the flame.

ISS experiments ($D_o > 1$ mm) show that soot production, as evidenced in the flame images by the intensity of its incandescence, *decreases* as D_o increases. This is attributed to the flame's lower

temperature due to increasing radiative heat losses from the gas phase. This decrease in flame temperature, marked by decreases in both flame luminosity and soot incandescence, results in a classical low gravity extinction phenomenon for droplet flame configurations, referred to as "radiative extinction" and is marked by the disappearance of the visible flame.

There is a threshold initial droplet diameter, for a given fuel and ambient atmosphere, below which the droplet will burn to near completion and extinguish diffusively[3] and above which the burning droplet will not achieve a quasi-steady burning phase and will radiatively extinguish shortly after ignition. This "radiative extinction threshold" initial diameter, $D_{o,rxt}$, is approximately 3 mm for the *n*-alkane fuels and chamber atmospheres reported in this work.

The precise value of $D_{o,rxt}$ is difficult to establish, as the droplet must remain completely motionless resulting in no relative gas phase velocity. It has been observed that the slightest droplet motion will result in a distortion of the spherical symmetry resulting in a reaction zone with a leading and trailing edge. In this situation fresh oxidizer is introduced to the reaction zone at the leading edge and the reaction zone at the trailing edge becomes limited in oxygen concentration and higher in product concentration. In these cases, when the initial diameter is near $D_{o,rxt}$ one will observe asymmetric or "localized flame extinction" at the trailing edge and, depending on the velocity of droplet (among other parameters) will "drive" the burning to completion; i.e., "diffusive extinction." However, when $D_o > D_{o,rxt}$, in a perfectly quiescent atmosphere, the spherical flame will rapidly reach a maximum diameter at which point its radiative losses, scaling approximately with D_f^3, will overwhelm the rate of energy released from combustion and result in a flame temperature below that necessary to sustain the reaction. Conversely, for droplets where $D_o < D_{o,rxt}$ the extinction mechanism is diffusively controlled and when the residence time of the fuel vapor in the reaction zone becomes less than the required reaction time a Damköhler extinction (i.e., "diffusive extinction") is observed. [3]

The flame extinction mechanisms, discussed above, are illustrated in the collection of images shown in Figs. 8–10. Tests with $D_o < D_{o,rxt}$ will typically show visible flames persisting for scaled times (i.e., t/D_o^2) greater than 0.6 s/mm². However, for those tests where $D_o > D_{o,rxt}$, visible flames will not exist for scaled times greater than 0.6 s/mm². For these larger droplet tests, only capable of being performed in ISS, extinction is triggered by excessive

---

[3] In a number of tests the droplet explodes just prior to diffusive flame extinction and current speculation raises the possibility of a mixture of dissimilar volatilities due to earlier dissolution of soot and/or soot pre-cursors at the droplet interface.
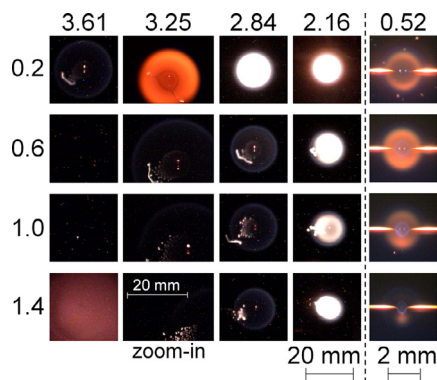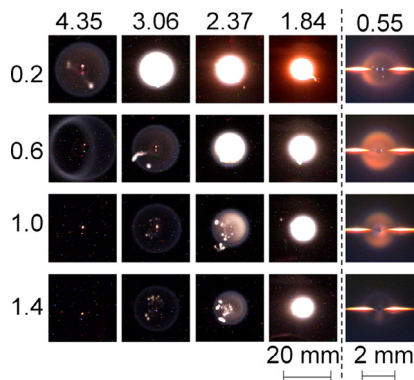
Fig. 9. Representative flame-illuminated images of burning n-octane droplets. Numbers across the top are D_o (mm); numbers in column are t/D_o^2 (s/mm^2). Images to the right of the dotted line are from a ground-based experiment (the droplets are supported) while images to the left are from space-based experiments (the droplets are free-floating). Note that the images from the space-based and ground-based experiments are scaled differently. A condensation cloud is visible at (3.61:1.4) after flame extinction. (For interpretation of the references to color in this figure, the reader is referred to the web version of this article).

Fig. 10. Representative flame-illuminated images of burning n-decane droplets. Numbers across the top are D_o (mm); numbers in column are t/D_o^2 (s/mm^2). Images to the right of the dotted line are from a ground-based experiment (the droplets are supported) while images to the left are from space-based experiments (the droplets are free-floating). Note that the images from the space-based and ground-based experiments are scaled differently. Image at (4.35:0.6) shows a large hole in the flame formed in the midst of radiative extinction. (For interpretation of the references to colour in this figure legend, the reader is referred to the web version of this article).

Fig. 11. Representative backlit black and white images of burning n-heptane droplets. Soot shells are visible in (3.55:0.2) and their evolution is shown in the subsequence images. Numbers across the top are D_o (mm); numbers in column are t/D_o^2 (s/mm^2). Images to the right of the dotted line are from a ground-based experiment (the droplets are supported) while images to the left are from space-based experiments (the droplets are free-floating). Note that the images from the space-based and ground-based experiments are scaled differently.

Fig. 12. Representative backlit black and white images of burning n-octane droplets. Soot shells are visible in (3.61:0.2) and their evolution is shown in subsequence images. Numbers across the top are D_o (mm); numbers in column are t/D_o^2 (s/mm^2). Images to the right of the dotted line are from a ground-based experiment (the droplets are supported) while images to the left are from space-based experiments (the droplets are free-floating). Note that the images from the space-based and ground-based experiments are scaled differently.

radiation losses from the gas phase such that combustion cannot be sustained [31,37,40,56]. Additionally, there are some instances, depending on fuel and ambient atmosphere, where immediately following radiative extinction of the visible flame the reaction will transition from a high temperature combustion (HTC) regime to a LTC regime. This is actually evidenced in some of the images presented Figs. 8–10 for the larger droplet diameter where, following a time lapse when there is no visible flame, the last image in Fig. 9 ($D_o = 3.61$ mm) shows a reddish-orange region due to fuel vapor condensation (see later discussion). In these cases, where LTC follows the visible flame's radiative extinction, the droplet will continue to burn until it is diffusively extinguished [37].

Precisely what characteristics of the experimental observations provide a definitive assessment of the extinction mechanism is speculative. The rate at which the flame disappears appears to be an important consideration [48]. For diffusive extinction the flame quickly disappears when evaporation is unable to sustain combustion. On the other hand, radiative extinction appears to be slower with the flame gradually disappearing before the droplet completely evaporates. This comparatively slow process is suggestive of other m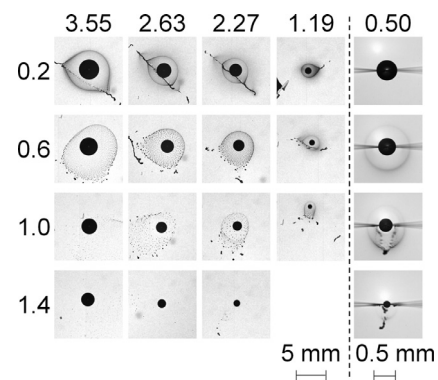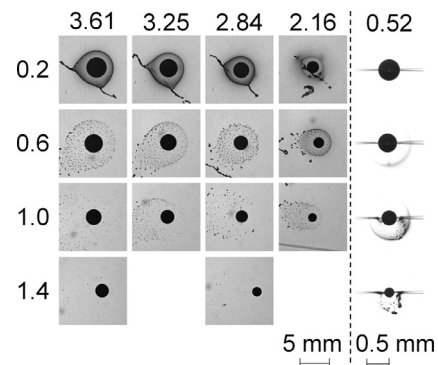echanisms that influence the extinction and LTC. It is noted that none of the small droplets investigated in the GB experiments exhibits radiative extinction.

Shortly after radiative extinction of octane and decane a cloud of condensed fuel vapor, similar to a fog, is observed as the backlighting, used for droplet imaging, is scattered by the presence of micron-sized fuel droplets. The phenomena, alternately referred to as the "vapor cloud" in earlier papers, is believed to serve as a marker for the termination of HTC, shown in Fig. 9 for those tests with $D_o > 3.5$ mm, where the fuel is no longer completely consumed by the hot flame. These "clouds" are believed to arise from condensation of fuel vapor as it leaks through the reaction zone during the extended LTC regime (though the cloud formation itself may not be necessarily relevant to the transition from HTC to LTC) and reaches a region in the far-field where temperatures fall below the fuel's boiling point.

Figures 11–13 show selected BW images of the burning histories of the same droplets shown in Figs. 8–10. The droplet and sooting dynamics are clearly visible (while in Figs. 8–10 soot incandescence obscures both due to the particular optical settings). For small droplets ($D_o < 1$ mm), the soot shell is almost intact throughout the burning process. For the larger droplets in the ISS, the soot shell intensity as qualitatively measured by the image darkness appears to become fainter as D_o increases. This trend is
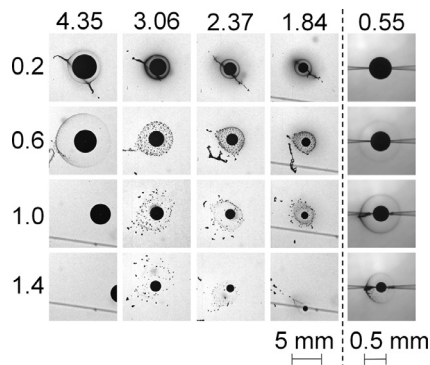
Fig. 13. Evolution of soot configuration for backlit photographs for *n*-decane droplets. Soot shells are visible in (4.35:0.2) and their evolution is shown in subsequence images. Numbers across the top are D_o (mm); numbers in column are t/D_o^2 (s/mm^2). Images to the right of the dotted line are from a ground-based experiment (the droplets are supported) while images to the left are from space-based experiments (the droplets are free-floating). Note that the images from the space-based and ground-based experiments are scaled differently.
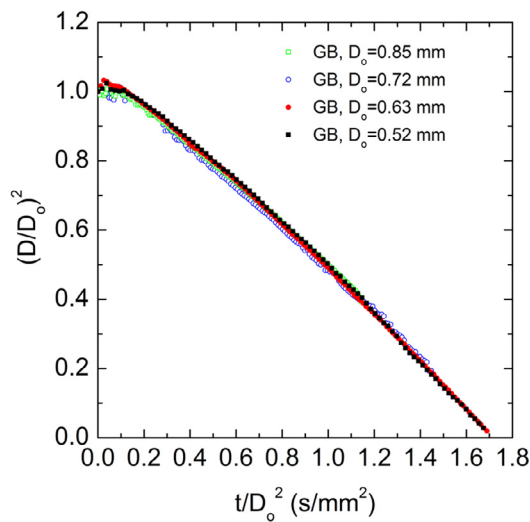
Fig. 14. Evolution of non-dimensional droplet diameter of *n*-octane for $D_o < 1$ mm. No influence of D_o on burning rate is apparent.

Fig. 15. (a) Evolution of scaled droplet diameter with scaled time for *n*-heptane. (b) Burning rates of pre-extinction data for $D_o > 2$ mm correlated as $K = 0.8531\ D_o^{-0.46}$.

consistent with Figs. 8–10 which show diminished flame luminosity as D_o increases.

The variation of $(D/D_o)^2$ with a normalized time (t/D_o^2) for octane is shown in Fig. 14 for $D_o < 1$ mm. The GB data ($D_o = 0.52$–0.85 mm) show virtually no influence of D_o. Earlier experiments which will suggest that radiative losses are minimal for D_o in this range (see Appendix A). The large droplet data (Figs. 15–17), however, suggest that the burning rate decreases with increasing D_o which is consistent with reduced sooting as D_o increases as noted in connection with Figs. 8–10. This trend is likely associated with radiative losses that sufficiently reduce the flame temperature to a point that it is below the soot inception temperature [57].

The quantitative measurements in Fig. 15 provide further evidence of extinction for large droplets: the burning rate rather noticeably decreases at some time during the burning history. The arrow in Fig. 15a marks the time for disappearance of the flame as discerned from the color images which are faintly noticed in Fig. 8. Thereafter, the burning rate is nearly linear with a lower rate.

In addition to a broad increase of burning rate with decreasing D_o shown in Figs. 15–17, within a given burning event the burning rate also increases as the burning process proceeds. This time dependence is likely due to unsteady heating that persists throughout the burning process [58,59]. In cases where an extinction-like
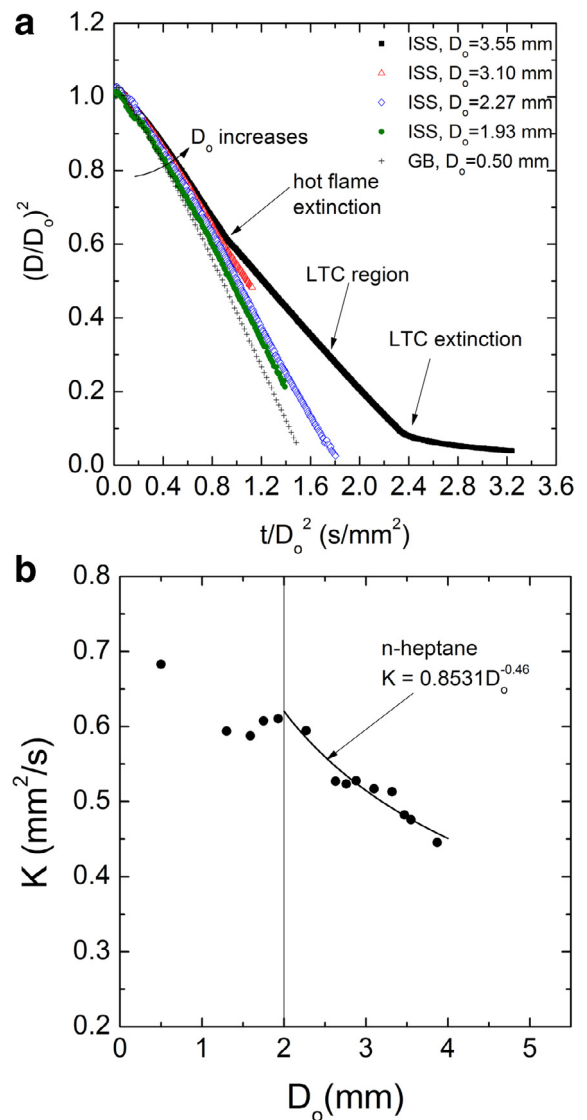
effect was found, the burning rate would ostensibly be expected to decrease because of reduced heat transfer to the droplet associated with disappearance of the flame, as shown in Figs. 15a and 16a (heptane and octane, respectively). These competing effects of droplet heating and post-extinction burning could result in either an increase or decrease of burning rate, at least for a time. Figure 17a for decane shows virtually no change in burning rate for $D_o = 4.35$ mm that is illustrated of this effect.

To clarify the influence of D_o on the burning rate, K was linearized using data in the initial (pre-extinction) regime of burning. Figures 15b–17b show the results. As shown in Figs. 15b–17b, the burning rates decreases with increasing D_o across the spectrum of droplet diameters investigated. This trend is consistent with reduced soot formation as D_o increases. The mechanism for this reduction appears to be increasing radiative losses as D_o increases, that in some cases eventually leads to radiative extinction noted previously. For the three alkanes investigated it appears that regime I in Fig. 2 corresponds approximately to $D_{oI} \sim 1$ mm, and in this range K does appear to exhibit an asymptotic trend which is consistent with the scaling arguments discussed previously (Appendix A). The experimental results suggest that
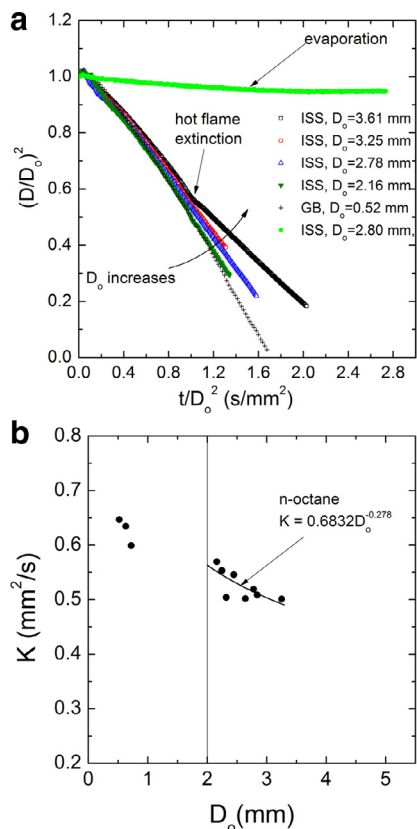
Fig. 16. (a) Evolution of scaled droplet diameter with scaled time for *n*-octane. (b) Burning rates of pre-extinction data for $D_o > 2$ mm correlated as $K = 0.6832\ D_o^{-0.278}$.

Fig. 17. (a) Evolution of scaled droplet diameter with scaled time for *n*-decane. (b) Burning rates of pre-extinction data for $D_o > 2$ mm correlated as $K = 1.1556\ D_o^{-0.779}$.

though soot formation is enhanced due to a larger t_{res} for $D_o > 1$ mm, radiative heat losses appear to overwhelmingly lower the flame temperature (hence inhibiting soot formation and reducing heat transfer to the droplet), leading to a decrease of burning rate with increasing D_o.

The arrows in Figs. 15a–17a point to the times at which a rather abrupt decrease of burning rate occurs. The burning rate after hot flame extinction (or radiative extinction) is still significantly higher than pure evaporation (cf. Fig. 16a, as indicated). The flame does not completely disappear at the time where the burning rate decreases, though the imaging diagnostics were insufficient to reveal the chemiluminescence of the faint flame that may still have been present. The post-radiative extinction zone is not predictable by high temperature (~2000 K) combustion kinetics. Rather, it appears to be controlled by low temperature (< 700–800 K [48]) combustion kinetics.

For some experiments an unusual oscillatory flame motion was observed that coincided with the sudden decrease in burning rate labeled as 'hot flame extinction' in Figs. 15a–17a. Figure 18 is a representative series of photographs of this effect. The numbers indicate the position of the image in the burning history. The first image (1) shows the flame at the start of its oscillation and images 2–18 in Fig. 18a show the process of the flame opening as extinction evolves. The flame starts to close at 18 and the process ends at 32 (Fig. 18b). This oscillatory flame motion resembles the motion of a 'jellyfish' and is referred to as jellyfish flame in some prior studies. Concurrently, radiative emissions exhibited an oscillatory behavior as shown in Fig. 19a by the wideband radiometer data (red line).

Previous studies that included discussion of flame oscillations predicted them for certain special conditions, for example burning in high temperature or pressure ambiences. A detailed numerical
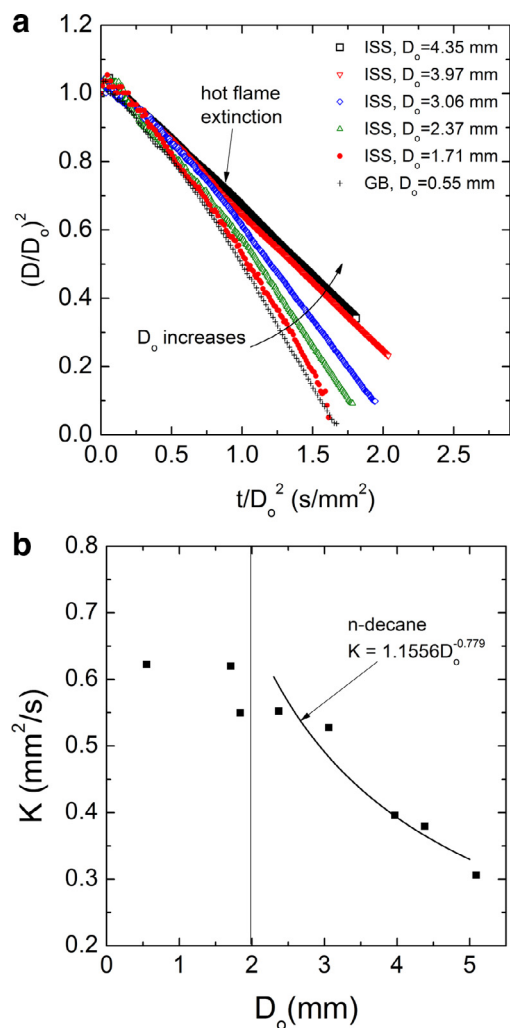
model of *n*-decane droplet burning in a high temperature ambience [38] showed that transition from high to low temperature burning was accompanied by an oscillating flame temperature. A detailed numerical model of droplet burning at elevated pressures [39] showed that multiple cycles of hot flame and LTC transitions for heptane were found at 3 atm along with oscillating peak gas temperatures. However, for burning in the standard atmosphere, flame oscillations (Fig. 18) were not predicted to occur.

A numerical model of this process was recently presented [60] in which flame oscillations were shown to be due to motion of the droplet that facilitated transport of oxygen to the stagnation point of the flame and depletion of oxygen in the wake of the flame that produced a 'hole' (e.g., image 28 in Fig. 18b) from which flame extinction originated. For a stationary droplet this sort of oscillatory flame motion is not predicted though the flame can, of course, still extinguish without oscillating.

Figure 19a shows D^2 data (grey symbols) along with wideband (red solid line) and narrowband (blue dashed line) radiometer data for an *n*-heptane droplet. This run was selected because it exhibits three regions in the burning history (recognized by different slopes): an early period where the flame is visible ('hot' flame region); an intermediate region where the flame is not visible but the burning rate is significantly higher than the evaporation rate associated with pure evaporation; and a third region where the evaporation rate is almost zero and evaporation has nearly ceased.

(a) flame open-up

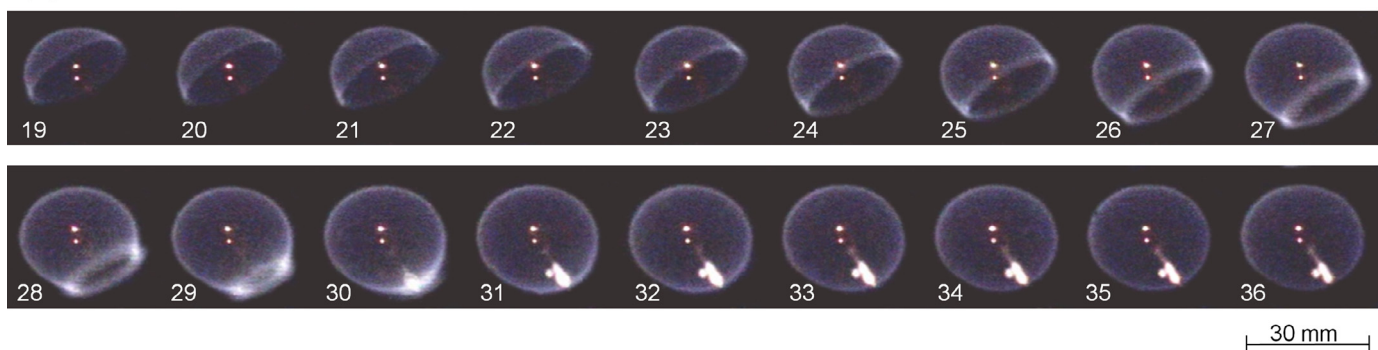## (b) flame close-back

30 mm
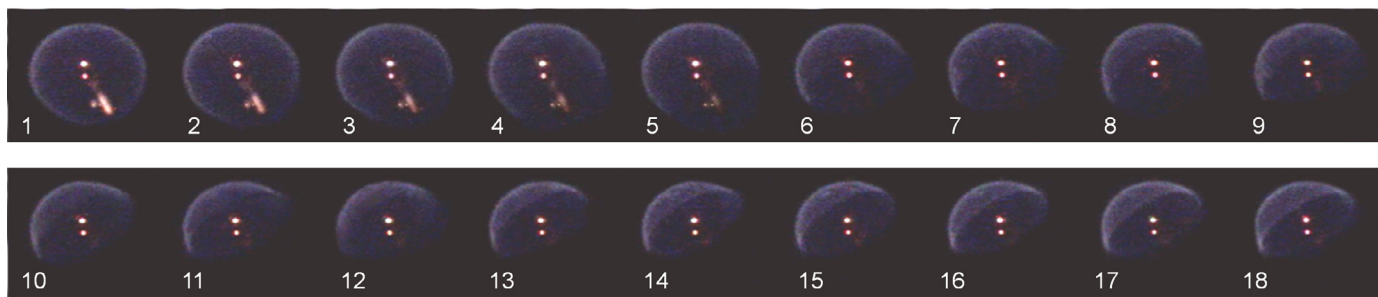
Fig. 18. Photographic sequence showing oscillations of a (blue) flame surrounding an *n*-decane droplet in the midst of experiencing radiative extinction. The increasing numbers at the left bottom corner of all images indicate the sequence of the event where the time between images is 1/30 s. (For interpretation of the references to colour in this figure legend, the reader is referred to the web version of this article).

The boundary (vertical dashed line) between the first two regions is believed to be associated with radiative extinction. Once in the second region the flame is not visible and the radiance significantly decreases yet the evaporation rate is still much larger than pure evaporation. This region is indicative of an LTC [37– 41]. Eventually the LTC region experiences extinction as evidenced by the reduction in evaporation to near pure evaporation at $t/D_o^2 \sim 2.4 \, s/mm^2$ as well as sudden decrease of narrowband signal that indicates water emission.

To illustrate the change in flame temperature due to radiative extinction, predicted flame temperature based on the scale analysis (Eq. (A12)) is shown in Fig. 19b, which illustrates the variation of predicted flame temperature commensurate with measured burning rates, D, D_f, and property estimates. The burning rate K is obtained by taking derivatives based on two adjacent data points in the D^2 plot (Fig. 19a) and the trend is processed by moving average and smooth functions in Matlab to reduce the noise and obtain a smooth curve of burning rate. It is seen that T_f is predicted to substantially drop at hot flame extinction to about 800 K in the LTC regime, and then to decrease to near room temperature after LTC.

Figure 20 shows the variation of D_{ext}/D_o with D_o for 2 mm < D_o < 5 mm, which is the range where radiative extinction was noted. For D_o < 3.25 mm, radiative extinction was not observed in any of the three fuels tested. The trends show that D_{ext}/D_o increases with D_o in a nearly linear manner and that the heavier alkane (i.e., *n*-decane) possesses a higher value for $D_{o,rxt}$; i.e., the droplet flames of lighter alkanes will tend to radiatively extinguish at smaller droplet diameters [37]. This observation is, in part, explained by recognizing that *n*-decane's boiling point is approximately 20% higher than *n*-heptane. The lower volatility of *n*-decane, given similar D_o's, results in a lower flame stand-

off (shown later) and commensurately smaller radiating gas phase volumes. Since it is the radiating volume of the gas phase which tends to drive the radiative extinction mechanism it seems reasonable that D_{ext}/D_o would increase as the flame diameter for a given D_o decreases, as is generally shown in the discussion that follows.

The evolution of flame standoff ratio (FSR $\equiv D_f/D$) for the three hydrocarbons is shown in Figs. 21–23. Twenty data points are presented for each ISS experiment while all GB flame images are measured and shown in these figures. The measurements clearly show that the gas phase transport processes are unsteady because the relative position of the flame to the droplet continually increases with time. This contrasts with the classical quasi-steady theory of droplet burning [2] which predicts that the FSR is constant and independent of time. The data also show that the FSR does not exhibit a regular variation with initial diameter. For example, a cross plot of the FSR in Figs. 21–23 with D_o for selected times during the burning history did not show consistent variation. The *n*-heptane and *n*-decane data showed that the FSR increased when D_o < 1.5 mm and decreased when D_o > 1.5 mm whereas the octane FSR decreased with increasing D_o for D_o < 1.0 mm.

Figures 24–26 present the evolution of soot standoff ratio, SSR $\equiv D_s/D$, for *n*-heptane, *n*-octane and *n*-decane. Following the conventional practice, we use the same normalized time scale for D_s as previously used for presenting the D and D_f data. The data show that the SSR increases with increasing D_o for the three alkanes. Though no theory currently exists for droplet burning that incorporates soot formation, prior qualitative modeling and scaling has shown that forces due to thermophoresis and drag (associated with fuel evaporation) are the dominant influences on trapping soot aggregates between the droplet and flame [3,12,15]. As such, viewing the thermophoretic forces on aggregates entirely from the perspec-
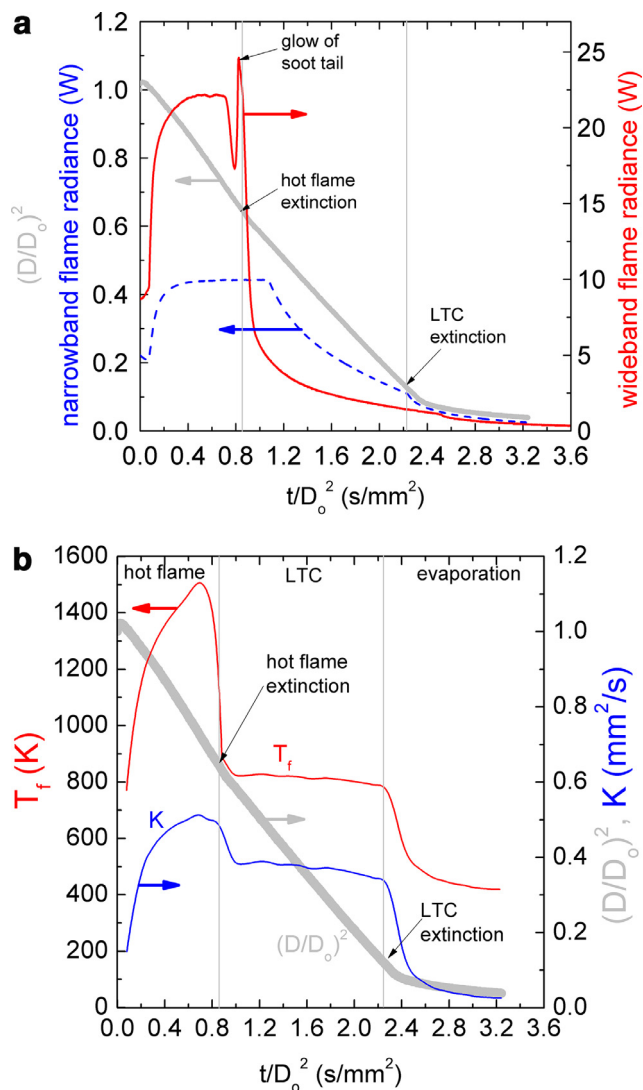
Fig. 19. (a) Evolution of measured narrowband (blue dashed line) and wideband (red solid line) flame radiances (W) for n-heptane ($D_o = 3.55$ mm). D^2 data (from Fig. 15a) are shown for reference. Extinction corresponds to disappearance of visible flame. (b) Predicted flame temperatures from scale analysis (Eq. (A12)) corresponding to measured burning rates and droplet diameters in (a) suggesting an LTC regime of burning followed by hot flame extinction. (For interpretation of the references to color in this figure legend, the reader is referred to the web version of this article).
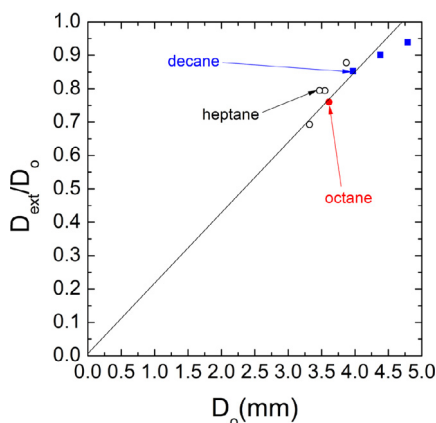
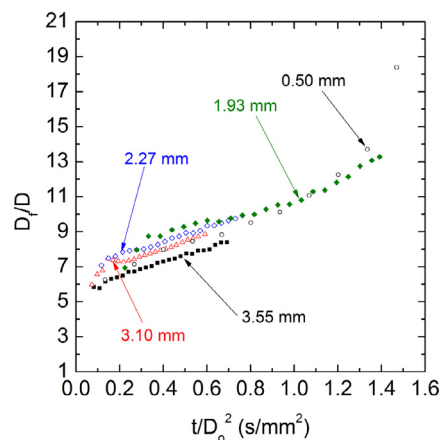**Fig. 20.** Variation of normalized extinction diameter (D_{ext}/D_o) with D_o.

Fig. 21. Evolution of flame standoff ratios (D_f/D) for selected D_o for n-heptane.
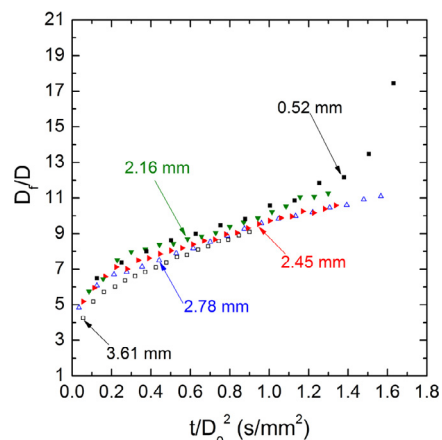

Fig. 22. Evolution of flame standoff ratios (D_f/D) for selected D_o for n-octane.
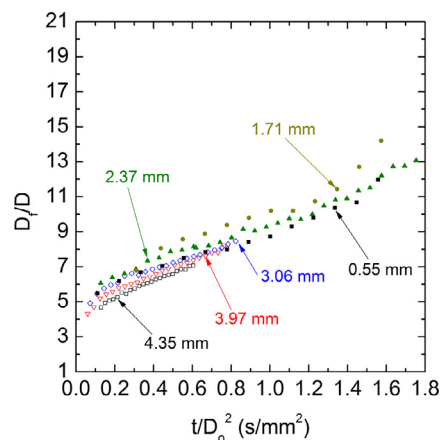

Fig. 23. Evolution of flame standoff ratios (D_f/D) for selected D_o for n-decane.

tive of the flame temperature, thermophoresis will decrease with D_o because the flame temperature also decreases. This effect will result in the SSR increasing with increasing D_o would be consistent with a lowering of thermophoretic forces on aggregates because the flame temperature reduces as D_o increases. Interestingly, in the post-extinction regime indicated in Fig. 26 (data enclosed by the dotted ellipse), the thermophoretic force would have to drop dramatically as the flame temperature is significantly lowered owing to the transition to low temperature chemistry. These trends need further study.
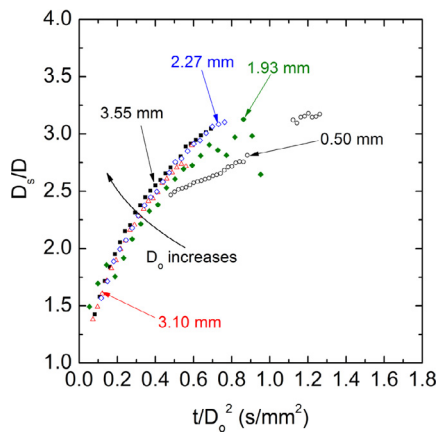
Fig. 24. Evolution of soot standoff ratio (D_s/D) for n-heptane droplet flames over the D_o range investigated.
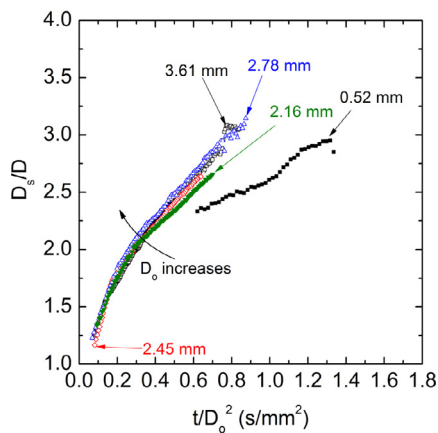

Fig. 25. Evolution of soot standoff ratio (D_s/D) for n-octane droplet flames over the D_o range investigated.
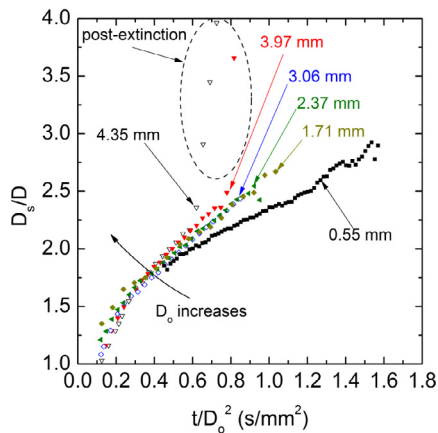

Fig. 26. Evolution of soot standoff ratio (D_s/D) for n-decane droplet flames over the D_o range investigated.

The data presented in this section are with representative conditions. The complete set of original data for droplet diameter history (Figs. 15–17, 19), D_{ext} (Fig. 20), FSR (Figs. 21–23) and SSR (Figs. 24–26) are available in the supplementary materials.

5. Conclusions

The influence of initial droplet diameter, D_o, on burning of single n-heptane, n-octane and n-decane droplets under micro-gravity conditions was examined to provide a better understanding for this dimension's effect on the combustion physics of spherically symmetric droplets. The effects of D_o are largely attributed to the interplay of soot formation and radiative heat losses, with the extent depending on the size of the D_o. The main findings in the present study are summarized as follows:

1. For n-octane, n-decane, and n-heptane droplets, with $D_o > 1$ mm, average burning rates (measured as the slope of $D^2(t)$ plotted with time), decrease with increases in D_o. This observation is in contrast to the widely held prediction from classical quasi-steady droplet combustion theory, which holds that burning rates are independent of D_o. This is largely due to the assumption that radiative effects are negligible in the formulation of the quasi-steady theory.

2. Three distinct stages of droplet evaporation were found for the single component fuels for $D_o > 3$ mm, with flame temperatures estimated from scale analysis being consistent with typical hot flame and LTC regimes of burning.

3. An oscillatory "jellyfish-like" flame motion was often found to occur near the point of radiative extinction often times during the transition period from the initial HTC regime and the LTC regime. This oscillatory behavior was generally the result of near-extinction flames in the presence of a relative gas phase velocity due to the uncontrolled motion of the droplet. As the weak flame was perturbed by the motion of the droplet in the quiescent ambient a partial formed "envelope flame" began to develop with an oxygen rich leading edge and a product rich trailing edge. Depending on the relative gas phase velocity feeding the flame front the flame and the size of the radiating volume, would either "radiatively extinguish" after one or more flame oscillations or grow stronger, due to the fresh oxygen supply at the leading edge, and subsequently burn to completion. Measurements from the wide band radiometers were able to detect the oscillations of the radiative emissions from the flame as it expanded and contracted.

4. The results suggest that FSR does not exhibit a regular variation with D_o. The measured increase of the SSR with D_o is thought to be due to a reduction in the thermophoretic forces on soot aggregates. It is likely that this results from a smaller temperature gradient due to a reduction in flame temperature from the higher radiative losses associated with increases in D_o.

5. A scaling argument was used to relate the average burning rate with initial droplet diameter that was in reasonably good agreement with the measurements.

Acknowledgments

Appendix A

A scale analysis is presented here that relates K to D_o. The assumptions include the following: radiation from the flame is
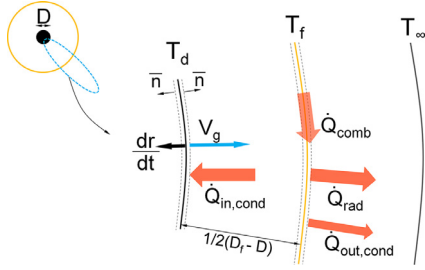
Fig. A1. Schematic of control volumes (dotted lines) used for energy balances at the droplet surface and flame.

mainly a loss mechanism to the ambience [8,23]; extinction is not considered (the existence of a 'hot' flame is presumed and we do not consider flames that arise by transitions to an LTC regime of burning); the gas is optically thin; the droplet diameter is scaled as D_o and thus C_F is scaled as D_f/D_o (except when experimentally measured D_f/D values are used to predict flame temperature); T_f (flame temperature) is much larger than T_∞ (far field temperature) (e.g., for heptane, $T_f \sim 2200$ K and $T_\infty \sim 300$ K); though the droplet flames form soot, this effect is not considered to influence the burning rate (e.g., an analysis that neglected soot formation yielded good agreement of burning rates for heptane [10]). We note that the data in Figs. 15b–17b show that K have a mild time-dependency indicative of droplet heating effects as noted earlier. In the following scaling analysis we assume that K is constant. Because the dependence of K on time is not very strong in the initial hot flame region prior to radiative extinction (see Figs. 15–17), we assume that K can be represented by an average value for each D_o in the analysis presented below; this was the basis for developing Figs. 15b–17b.

With reference to Fig. A1, an energy balance on the *flame* gives

$$\dot{Q}_{comb} \sim \dot{Q}_{in,cond} + \dot{Q}_{rad} + \dot{Q}_{out,cond}. \tag{A1}$$

Assuming that all of the fuel transported to the flame is reacted,

$$\dot{Q}_{comb} \sim \dot{m}_F \Delta H_c. \tag{A2}$$

The fuel evaporation (at a rate of $\dot{m}_F$) is sustained by the heat transferred inward from the flame to the droplet:

$$\dot{Q}_{in,cond} \sim \dot{m}_F h_{fg}. \tag{A3}$$

The fuel mass evaporation rate is taken from the classical theory of droplet combustion [2]

$$\dot{m}_F \sim \frac{1}{4}\pi \rho_L D_o K \tag{A4}$$

Regarding $\dot{Q}_{out,cond}$, the flame is modeled as a semi-infinite surface at temperature T_f with a characteristic time scale for heat diffusion from the flame to the ambience as $\frac{D_o^2}{K}$ so that

$$\dot{Q}_{out,cond} \sim \sqrt{\frac{\pi K}{\wp_g}} k_g T_f C_F^2 D_o, \tag{A5}$$

Unity Lewis number is assumed in Eq. (A5). For the overall radiative heat transfer rate from the flame to the ambience the approximation of [8] is used: $\dot{Q}_{rad} \sim \pi \varepsilon_g \sigma T_f^4 C_F^2 D_o^2$. Using the optically thin form of Beer's law with an optical path length as the flame diameter – $\varepsilon_g \sim \kappa_g C_F D_o$ – gives Eq. (A6)

$$\dot{Q}_{rad} \sim \pi \kappa_g \sigma T_f^4 C_F^3 D_o^3 \tag{A6}$$

With Eqs. (A1)–(A6), the droplet burning rate can be related to parameter as

$$K \sim \frac{4\kappa_g \sigma C_F^3 D_o^2 T_f^4}{\rho_L(\Delta H_c - h_{fg})} \left[1 + \sqrt{\frac{K}{\pi \wp_g}} \frac{k_g}{C_F \kappa_g \sigma D_o^2 T_f^3} \right] \tag{A7}$$

We consider two limits for Eq. (A7).

For $\dot{Q}_{rad} \gg \dot{Q}_{out,cond}$ the second term in brackets in Eq. (A7) is negligible:

$$K \sim \frac{4\kappa_g \sigma C_F^3 D_o^2 T_f^4}{\rho_L(\Delta H_c - h_{fg})} \tag{A8}$$

T_f in Eq. (A8) is scaled as averaged gas temperature and thus eliminated by noting that from the classical theory of droplet combustion [2] $K \sim \frac{\rho_g \wp_g}{\rho_L}$ and that [44] $\rho_g \wp_g \sim C_D(M_W T_f)^{1/2}$ so that

$$T_f \sim \left(\frac{K \rho_L}{C_D} \right)^2 \frac{1}{M_W} \tag{A9}$$

Note that the molecular weight in Eq. (A9) is the averaged molecular weight of the fuel-air mixture.

Substituting Eq. (A9) into Eq. (A8),

$$K \sim \left(\frac{(\Delta H_c - h_{fg})C_D^8 M_W^4}{4C_F^3 \kappa_g \sigma} \right)^{1/7} \frac{1}{\rho_L D_o^{2/7}} \tag{A10}$$

where it is seen that $K \sim \rho_L^{-1} D_o^{-2/7}$ which shows the importance of liquid density and droplet size on K in the limit of dominant radiative losses.

When radiation is negligible ($\dot{Q}_{rad} \ll \dot{Q}_{out,cond}$) the second term in Eq. (A7) dominates. Upon substituting Eq. (A9) for T_f and solving for K gives

$$K \sim \left(\frac{(\Delta H_c - h_{fg})(\pi \wp_g)^{1/2} M_W C_D^2}{4C_F^2 k_g \rho_L} \right)^{2/3} \tag{A11}$$

where now K does not depend on D_o when radiation is negligible, which is consistent with detailed numerical modeling in this limit [8,13]. From the above scaling the variation of burning rate with initial droplet diameter may be traced to the influence of radiative losses from the droplet flame. These qualitative trends of how K depends on D_o are consistent with the data shown in Figs. 19–21.

The predicted flame temperature values presented in Fig. 19b are obtained by a mass and energy balance at the droplet surface that equates enthalpy transport to conduction at the droplet surface. A gas velocity V_g from fuel evaporation transports enthalpy in the region between the droplet and flame. The energy balance at the droplet surface results in $\frac{\partial T}{\partial r}|_{r=D/2} = \frac{1}{4}\frac{\rho_L h_{fg}}{k_g}\frac{K}{D}$. Scaling the derivative as $\frac{\partial T}{\partial r} \sim 2\frac{T_f - T_d}{D_f - D}$ gives a relationship between T_f, D_f, D and K as

$$T_f \sim T_d + \frac{1}{8}\left(\frac{D_f}{D} - 1 \right)\frac{\rho_L h_{fg}}{k_g}K \tag{A12}$$

From measured values of K, D_f and D at each instant during droplet burning, Eq. (A12) provides a means to estimate the corresponding flame temperature. Applying Eq. (A12) to the heptane data in Fig. 19b shows that the flame temperature drops significantly and reaches values which are consistent with a LTC regime of burning as discussed in Section 4.

Supplementary materials

Supplementary material associated with this article can be found, in the online version, at doi:10.1016/j.combustflame.2016.05.013.

References

[1] W.A. Sirignano, Fluid dynamics and transport of droplets and sprays, Cambridge University Press, 1999, pp. 23–76.
[2] S.R. Turns, An introduction to combustion, second ed., McGraw-Hill Inc, 2006, p. 391. Chapter 10 Appendix B.
[3] G.S. Jackson, C.T. Avedisian, J.C. Yang, Observations of soot during droplet combustion at low gravity: heptane and heptane/monochloroalkane mixtures, Int. J. Heat Mass Transf. 35 (1992) 2017–2033.

[4] C.T. Avedisian, Soot formation in spherically symmetric droplet combustion, Physical and Chemical Aspects of Combustion, Gordon and Breach Publ., 1997, pp. 135–160.

[5] C.K. Law, W.A. Sirignano, Unsteady droplet combustion with droplet heating—II: conduction limit, Combust. Flame 28 (1977) 175–186.

[6] C.K. Law, H.K. Law, A d2-law for multicomponent droplet vaporization and combustion, AIAA J. 20 (1982) 522–527.

[7] W.A. Sirignano, Fuel droplet vaporization and spray combustion theory, Prog. Energy Combust. Sci. 9 (1983) 291–322.

[8] A.J. Marchese, F.L. Dryer, The effect of non-luminous thermal radiation in microgravity droplet combustion, Combust. Sci. Technol. 124 (1997) 371–402.

[9] T.I. Farouk, F.L. Dryer, On the extinction characteristics of alcohol droplet combustion under microgravity conditions – a numerical study, Combust. Flame 159 (2012) 3208–3223.

[10] T.I. Farouk, Y.C. Liu, A.J. Savas, C.T. Avedisian, F.L. Dryer, Sub-millimeter sized methyl butanoate droplet combustion: microgravity experiments and detailed numerical modeling, Proc. Combust. Inst. 34 (2013) 1609–1616.

[11] Y.C. Liu, T. Farouk, A.J. Savas, F.L. Dryer, C.T. Avedisian, On the spherically symmetrical combustion of methyl decanoate droplets and comparisons with detailed numerical modeling, Combust. Flame 160 (2013) 641–655.

[12] G. Ben-Dor, T. Elperin, B. Krasovitov, Effect of thermo – and diffusiophoretic forces on the motion of flame-generated particles in the neighbourhood of burning droplets in microgravity conditions, Proc. R. Soc. A 459 (2003) 766–703.

[13] G.S. Jackson, C.T. Avedisian, Modeling of spherically symmetric droplet flames including complex chemistry: effect of water addition on *n*-heptane droplet combustion, Combust. Sci. Technol. 115 (1996) 125–149.

[14] S.L. Manzello, M.Y. Choi, A. Kazakov, F.L. Dryer, R. Dobashi, T. Hirano, The burning of large *n*-heptane droplets in microgravity, Proc. Combust. Inst. 28 (2000) 1079–1086.

[15] S. Kumar, A. Ray, S.R. Kale, A soot model for transient, spherically symmetric *n*-heptane droplet combustion, Combust. Sci. Technol. 174 (2002) 67–102.

[16] S. Kumagai, T. Sakai, S. Okajima, Combustion of free fuel droplets in a freely falling chamber, Symp. (Int.) Combust. 13 (1971) 779–785.

[17] G.S. Jackson, C.T. Avedisian, The effect of initial diameter in spherically symmetric droplet combustion of sooting fuels, Proc. R. Soc. A 446 (1994) 255–276.

[18] H. Hara, S. Kumagai, The effect of initial diameter on free droplet combustion with spherical flame, Symp. (Int.) Combust. 25 (1994) 423–430.

[19] K.-O. Lee, S.L. Manzello, M.Y. Choi, The effects of initial diameter on sooting and burning behavior of isolated droplets under microgravity conditions, Combust. Sci. Technol. 132 (1998) 139–156.

[20] G. Xu, M. Ikegami, S. Honma, K. Ikeda, X. Ma, H. Nagaishi, D.L. Dietrich, P.M. Struk, Inverse influence of initial diameter on droplet burning rate in cold and hot ambiences: a thermal action of flame in balance with heat loss, Int. J. Heat Mass Transf. 46 (2003) 1155–1169.

[21] G. Xu, M. Ikegami, S. Honma, K. Ikeda, D.L. Dietrich, P.M. Struk, Sooting characteristics of isolated droplet burning in heated ambients under microgravity, Int. J. Heat Mass Transf. 47 (2004) 5807–5821.

[22] G. Xu, M. Ikegami, S. Honma, K. Ikeda, D.L. Dietrich, P.M. Struk, Interactive influences of convective flow and initial droplet diameter on isolated droplet burning rate, Int. J. Heat Mass Transf. 47 (2004) 2029–2035.

[23] K.C. Chang, J.S. Shieh, Theoretical investigation of transient droplet combustion by considering flame radiation, Int. J. Heat Mass Transf. 38 (1995) 2611–2621.

[24] A.J. Marchese, F.L. Dryer, V. Nayagam, Numerical modeling of isolated *n*-alkane droplet flames: initial comparisons with ground and space-based microgravity experiments, Combust. Flame 116 (1999) 432–459.

[25] A.J. Marchese, F.L. Dryer, R.O. Colantonio, Radiative effects in space-based methanol/water droplet combustion experiments, Symp. (Int.) Combust. 27 (1998) 2627–2634.

[26] V. Nayagam, J.B. Haggard Jr., R.O. Colantonio, A.J. Marchese, F.L. Dryer, B.L. Zhang, F.A. Williams, Microgravity *n*-heptane droplet combustion in oxygen-helium mixtures at atmospheric pressure, AIAA J. 36 (1998) 1369–1378.

[27] Y.C. Liu, Droplet combustion of surrogate and real fuel systems in a low convection condition: ground-based and space-based experiments (Ph.D. Dissertation), Sibley School of Mechanical and Aerospace Engineering, Cornell University, Ithaca, NY, USA, 2013.

[28] G.S. Jackson, C.T. Avedisian, J.C. Yang, Soot formation during combustion of unsupported methanol/toluene mixture droplets in microgravity, Proc. R. Soc. Lond. A 435 (1991) 359–369.

[29] J.H. Bae, C.T. Avedisian, , Experimental study of the combustion dynamics of jet fuel droplets with additives in the absence of convection, Combust. Flame 137 (2004) 148–162.

[30] J. Bae, Experimental Observations and Analyses on the Dynamics of Isolated Spherical Droplet Flames Burning in Various Ambient Gases and Pressures (Ph.D. Dissertation), Sibley School of Mechanical and Aerospace Engineering, Cornell University, Ithaca, NY, USA, 2005.

[31] A. Kazakov, J. Conley, F.L. Dryer, Detailed modeling of an isolated, ethanol droplet combustion under microgravity conditions, Combust. Flame 134 (2003) 301–314.

[32] A. Bejan, Convection heat transfer, third ed., John Wiley, 2004, pp. 19–23.

[33] V. Nayagam, A.J. Marchese, K.R. Sacksteder, Microgravity droplet combustion: An inverse scale modeling problem, in: K. Saito (Ed.), Progress in Scale Modeling, Springer, 2008, pp. 169–178.

[34] C. Presser, A.K. Gupta, C.T. Avedisian, H.G. Semerjian, Fuel property effects on the structure of spray flames, Symp. (Int.) Combust. 23 (1991) 1361–1367.

[35] B.H. Chao, C.K. Law, J.S. T'ien, Structure and extinction of diffusion flames with flame radiation, Symp. (Int.) Combust. 23 (1990) 523–531.

[36] C.T. Avedisian, C. Presser, A.K. Gupta, Observations of soot in the combustion of methanol/toluene spray flames, J. Propulsion. Power 18 (2002) 781–787.

[37] V. Nayagam, D.L. Dietrich, M.C. Hicks, F.A. Williams, Cool-flame extinction during n-alkane droplet combustion in microgravity, Combust. Flame 162 (2015) 2140–2147.

[38] A. Cuoci, A. Frassoldati, T. Faravelli, E. Ranzi, Numerical modeling of auto-ignition of isolated fuel droplets in microgravity, Proc. Combust. Inst. 35 (2015) 1621–1627.

[39] T.I. Farouk, M.C. Hicks, F.L. Dryer, Multistage oscillatory "Cool Flame" behavior for isolated alkane droplet combustion in elevated pressure microgravity condition, Proc. Combust. Inst. 35 (2015) 1701–1708.

[40] V. Nayagam, D.L. Dietrich, P.V. Ferkul, H.C. Hicks, F.A. Williams, Can cool flames support quasi-steady alkane droplet burning? Combust. Flame 159 (2012) 3583–3588.

[41] T. Farouk, F.L. Dryer, Isolated n-heptane droplet combustion in microgravity: "Cool Flames" – two-stage combustion, Combust. Flame 161 (2014) 565–581.

[42] A. Cuoci, M. Mehl, G. Buzzi-Ferraris, T. Faravelli, D. Manca, E. Ranzi, Autoignition and burning rates of fuel droplets under microgravity, Combust. Flame 143 (2005) 221–226.

[43] Y.C. Liu, C.T. Avedisian, A comparison of the spherical flame characteristics of sub-millimeter droplets of binary mixtures of n-heptane/iso-octane and n-heptane/toluene with a commercial unleaded gasoline, Combust. Flame 159 (2012) 770–783.

[44] R.C. Reid, J.M. Prausnitz, T.K. Sherwood, The properties of gases and liquids, 3rd ed., McGraw-Hill, 1977, p. 59. Chapter 3 and Appendix A.

[45] D.L. Dietrich, J.B. Haggard Jr., F.L. Dryer, V. Nayagam, B.D. Shaw, F.A. Williams, Droplet combustion experiments in spacelab, Symp. (Int.) Combust. 26 (1996) 1201–1207.

[46] B. Banu, Fluids and combustion facility (FCF) and combustion integrated rack (CIR), Payload Accommodations Handbook CIR-DOC-4064, NASA John H. Glenn Research Center, Cleveland, Ohio, 2008.

[47] J. Robbins, C. Shinn, Multi-user droplet combustion apparatus flex2, Reflight Safety Data Package MDC-DOC-1790A, NASA John H. Glenn Research Center, Cleveland, Ohio, 2010.

[48] D.L. Dietrich, V. Nayagam, H.C. Hicks, P.V. Ferkul, F.L. Dryer, T. Farouk, B.D. Shaw, H.-K. Suh, M.Y. Choi, Y.C. Liu, C.T. Avedisian, F.A. Williams, Droplet combustion experiments aboard the international space station, Microgravity Sci. Technol. 26 (2014) 65–76.

[49] C.T. Avedisian, Recent advances in soot formation from spherical droplet flames at atmospheric pressure, J. Propulsion. Power 16 (2000) 628–635.

[50] C.T. Avedisian, J.C. Yang, C.H. Wang, On low-gravity droplet combustion, Proc. R. Soc. Lond. A 420 (1988) 183–200.

[51] J.C. Yang, C.T. Avedisian, The combustion of unsupported heptane/hexadecane mixture droplets at low gravity, Symp. (Int.) Combust. 22 (1989) 2037–2044.

[52] Y.C. Liu, Y. Xu, C.T. Avedisian, M.C. Hicks, The effect of support fibers on micro–convection in droplet combustion experiments, Proc. Combust. Inst. 35 (2015) 1709–1716.

[53] C.L. Dembia, Y.C. Liu, C.T. Avedisian, Automated data analysis for consecutive images from droplet combustion experiments, Image Anal. Stereol. 31 (2012) 137–148.

[54] B. Knight, F.A. Williams, Observations on the burning of droplets in the absence of buoyancy, Combust. Flame 38 (1980) 111–119.

[55] M.Y. Choi, F.L. Dryer, G.J. Green, J.J. Sangiovanni, Soot agglomeration in isolated, free droplet combustion, 31st Aerospace Sciences Meeting & Exhibit (1993), Reno, Nevada, AIAA Paper No. 93-0823.

[56] M.C. Hicks, V. Nayagam, F.A. Williams, Methanol droplet extinction in carbon–dioxide-enriched environments in microgravity, Combust. Flame 157 (2010) 1439–1445.

[57] R.A. Dobbins, Soot inception temperature and the carbonization rate of precursor particles, Combust. Flame 130 (2002) 204–214.

[58] C.T. Avedisian, B.J. Callahan, Experimental study of nonane/hexanol mixture droplet combustion without natural or forced convection, Proc. Combust. Inst. 28 (2000) 991–997.

[59] B.D. Shaw, F.A. Williams, Theory of influence of a low-volatility, soluble impurity on spherically-symmetric combustion of fuel droplets, Int. J. Heat Mass Transf. 33 (1990) 301–317.

[60] F. Takahashi, V.R. Katta, M.C. Hicks, Combustion characteristics in a non-premixed cool-flame regime of n-heptane in microgravity, 9th U.S. National Combustion Meeting, Central Section of the Combustion Institute, May 17–20, Cincinnati, Ohio, USA, 2015 Paper No. 3E02.